

pubs.acs.org/JPCC Article

Revealing Stability of Inverted Planar MA-Free Perovskite Solar Cells and Electric Field-Induced Phase Instability

Erjin Zheng, Zhiyin Niu, Gabriella A. Tosado, Hao Dong, Yaqoub Albrikan, and Qiuming Yu*



Cite This: J. Phys. Chem. C 2020, 124, 18805-18815



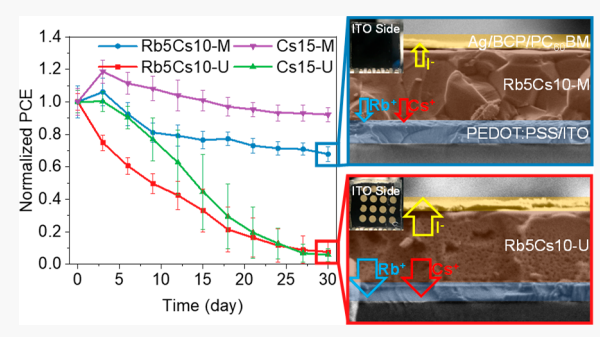
ACCESS

III Metrics & More

Article Recommendations

3 Supporting Information

ABSTRACT: Hybrid organic—inorganic perovskite is one of the most promising candidates to replace state-of-art silicon to fabricate low cost solar cells. However, its instability, including intrinsic and operational instability, strongly hinders its real-life applications. Methylammonium (MA)-free, formamidinium (FA)-based perovskite doped by small A-site inorganic cations was developed to tackle the intrinsic instability issue, but the operational instability, especially against the applied electric field, induced by defect mediated ion migration remains a problem. In this work, we fabricate two types of MA-free perovskites, Rb_{0.05}Cs_{0.1}FA_{0.85}PbI₃ and Cs_{0.15}FA_{0.85}PbI₃, and investigate the effect of Rb⁺ on the device performance and long-term stability. We find that even with incomplete incorporation, Rb⁺ cation can significantly improve the device perform-



ance. We reveal the defect-mediated cation and anion migration under electric field using cross-sectional secondary electron microscopy, X-ray photoelectron spectroscopy, and time-of-flight secondary ion mass spectrometry, and identify that Rb⁺ is more vulnerable compared to Cs^+ . By simply mixing the precursor solution before spin coating, we significantly reduce the defect states in both types of perovskite and improve the device stability against an electric field. The modified precursor solution provides the devices with $Rb_{0.05}Cs_{0.1}FA_{0.85}PbI_3$ and $Cs_{0.15}FA_{0.85}PbI_3$ active layers that retain 68% and 92% of their initial PCE, respectively, over 30 days under N_2 protection.

■ INTRODUCTION

Methylammonium lead triiodide (MAPbI₃) perovskite is one of the most studied perovskites, and a PCE as high as 20% has been demonstrated for single junction solar cells. 1-3 However, MAPbI₃ perovskite is not an ideal option to fabricate high performance and stable single junction perovskite solar cells mainly due to its intrinsic moisture and thermal instability.^{4–8} Formamidinium (FA) as another organic cation has been applied as a replacement for MA to solve the instability issues. However, FAPbI₃ suffers from phase instability under room temperature. It spontaneously transfers from a black photoactive α -phase to a yellow photoinactive δ -phase at room temperature in a few days.¹⁰ To solve the phase instability problem, alkaline cation such as Cs+ and Rb+ cations are introduced to partially replace the large FA cation to adjust the Goldschmidt tolerance factor. 11-20 Compared with the wellstudied Cs^+ cation, the incorporation of $R\bar{b}^+$ in $FAPbI_3$ and the effect of Rb+ on phase stability and device performance remains unclear. There are a few works regarding Rb-doped MA-free perovskite solar cells and all are in the conventional device structure. 18,20

Beyond the intrinsic phase stability problem, ion migration induced operational degradation is another critical factor that prevents the commercialization of perovskite solar cells. ^{21–25} Ion migration has been observed in both single component and mixed-cation/-halide perovskites, where the A-site cation

and the X-site halide with low activation energy migrate spontaneously or upon stimulation. Higher energy irradiance, temperature, and electric field have been reported to trigger the ion migration.²⁶ Ion migration must be mediated by the defects in the perovskite solid films, such as Schottky and Frenkel defects and grain boundaries.^{27,28} In order to thoroughly prevent the degradation and meet the real-life usage requirement, it is highly desired to fabricate MA-free perovskites with reduced defect densities.

In this work, we purposely selected mixed Cs^+ and Rb^+ and single Cs^+ as the A-site cation dopants to fabricate two types of MA-free perovskites, $Rb_{0.05}Cs_{0.1}FA_{0.85}PbI_3$ and $Cs_{0.15}FA_{0.85}PbI_3$, and investigated the effect of Rb^+ cations on device performance and long-term stability against electric field of inverted structured MA-free perovskite solar cells. We investigated the ion migration under electric field, such as the area under the electrode, and without electric field, such as the area between electrodes, and its impact on perovskite phase

Received: June 12, 2020 Revised: August 2, 2020 Published: August 3, 2020





segregation and device stability. In addition, we varied the precursor preparation methods to effectively control the defect densities in the resulted perovskite films, which not only impacts the device performance but also the device stability. This work sheds light on the development of MA-free perovskite solar cells by reducing defects and electric field induced ion migration.

EXPERIMENTAL SECTION

Materials. Indium tin oxide (ITO) coated glass (sheet resistance = $10 \ \Omega \cdot \text{sq}^{-1}$) was purchased from Colorado Concept Coating, LLC. Poly(3,4-ethylenedioxythiophene):polystyrenesulfonate (PEDOT:PSS, CLEVIOS P VP AI 4083) was purchased from Heraeus. Lead iodide (PbI₂, for perovskite precursor, 99.99%) was purchased from Tokyo Chemical Industry. Formamidinium iodide (FAI) was purchased from Greatcell Solar. Ag evaporation pellets (99.999%) were purchased from R.D. Mathis. Dimethyl sulfoxide (DMSO, anhydrous, $\geq 99.9\%$), N,N-Dimethylformamide (DMF, anhydrous, $\geq 99.8\%$), chloroform (anhydrous, $\geq 99\%$), 2-propanol (anhydrous, 99.5%), bathocuproine (BCP, 96%), diethyl ether (DEE, $\geq 99.0\%$), RbI (99.9%), and CsI (99.999%) were purchased from Sigma-Aldrich. All the materials were used as-received without further purification.

Thin Film Fabrication. Perovskite precursors were prepared as follows: PbI₂ (1.1 M) was dissolved in DMF:DMSO 4:1 (v/v) by stirring at 80 °C for 1 h. PbI2 (1.1 M) solution was added into RbI (1 M), CsI (1 M), and FAI (1 M) to form RbPbI₃, CsPbI₃, and FAPbI₃ precursor solutions. RbPbI₃ and FAPbI₃ solutions were stirred at room temperature for 1 h. CsPbI₃ solution was stirred at 80 °C for \sim 3.5 min then room temperature for 1 h. Rb_{0.05}Cs_{0.1}FA_{0.85}PbI₃ and Cs_{0.15}FA_{0.85}PbI₃ precursor solutions were prepared by mixing the desired volumetric ratios of the above solutions. The final precursor solution was stirred at room temperature overnight and passed 0.45 µm PTFE filter. Glass substrates were cut into 1.5×1.5 cm² pieces, then cleaned by sonication in soapy deionized (DI) water, DI water, acetone, and isopropanol for 15 min each sequentially and finally treated with 100 W oxygen plasma for 10 min. PEDOT:PSS was spin coated onto the cleaned glass substrate at 5000 rpm (ramp: 5000 rpm/s) for 60 s, followed by annealing at 150 °C for 10 min in the ambient condition. The substrates were then transferred into a N2 filled glovebox. The substrates and precursor solution were placed on a 70 °C hot plate and the precursors were either stirred under 500 rpm or unstirred. The heated substrate was transferred onto the spin coater, and the hot precursor solution was dropped onto the substrate. The substrate was spun at 1000 rpm for 10 s (ramp: 200 rpm/s) and 4000 rpm for 30 s (ramp: 4000 rpm/s). A 300 μ L of DEE was dropped onto the substrate at the last 10 or 15 s of the entire process for Rb_{0.05}Cs_{0.10}FA_{0.85}PbI₃ and Cs_{0.15}FA_{0.85}PbI₃, respectively. The substrates were annealed at 100 °C for 10 min.

Thin Film Characterization. Scanning electron microscopy (SEM) and energy dispersive spectroscopy (EDS) were acquired using a FEI Sirion SEM to investigate the surface morphology and elemental compositions of perovskite thin films, respectively. Two-dimensional X-ray diffraction (XRD) patterns were performed on a Bruker D8 Discover with I μ S 2-D XRD System using Cu K α radiation (λ = 1.54184 Å). Crosssectional SEM was performed on TFS Apreo-S without any sample pretreatment. Ultraviolet—visible (UV—vis) absorption

spectra were collected via a Varian Cary 5000 UV-vis-NIR spectrophotometer. Ultraviolet photoelectron spectroscopy (UPS) measurements were performed on a Kratos AXIS Ultra DLD spectrometer. A He discharge lamp source (Kratos) at an excitation energy of 21.2 eV was used in combination with a delay line detector at an electron pass energy of 5 eV. The UPS spectra for Au were acquired with a step size of 0.1 eV and a dwell time of 100 ms. The high-resolution UPS spectra and Fermi edge spectra were acquired with a step size of 0.01 eV and a dwell time of 100 ms. X-ray photoelectron spectroscopy (XPS) measurements were performed on a Kratos AXIS Ultra DLD X-ray photoelectron spectrometer. The incident X-rays were monochromatized Al K α (KE = 1486.6 eV) operated at 10 mA and 15 kV. All XPS data were acquired at a normal photoelectron takeoff angle of 0°. The survey spectra were acquired with a step size of 1.0 eV and a dwell time of 100 ms at a spectrometer pass energy of 160 eV. The high-resolution spectra were acquired with a step size of 0.1 eV and a dwell time of 425 ms for S 2p spectra and 259 ms for C 1s spectra at a spectrometer pass energy of 40 eV. Data analysis was performed using Kratos Vision Processing software (ver. 2.2.8). The binding energy scale was calibrated by assigning the lowest binding energy C 1s peak to 285.0 eV. All samples were measured under ultrahigh vacuum of around 5×10^{-9} Torr. The probing depth for both UPS and XPS was approximately 10 nm. Time-of-flight secondary ion mass spectrometry (ToF-SIMS, ION-TOF) was applied to gain the depth profile after the devices have been undergoing the stability tests. A beam of Ar₁₀₀₀ with 10 keV (4.4 nA) was applied for depth profiling on a raster area of 300 \times 300 μ m². A Bi³⁺ primary beam (0.01 pA) was scanned over a 100×100 μ m² area. The data are normalized by the measured total ion counts to eliminate the artifacts from a charging ion yield in different lavers.

Device Fabrication. ITO coated glass substrates with the size of $1.5\times1.5~{\rm cm}^2$ were cleaned following the same cleaning procedure as glass substrates. PEDOT:PSS and perovskite layers were fabricated as described in the thin film fabrication section. A 60 $\mu{\rm L}$ drop of PC $_{60}$ BM solution (15 mg/mL in chloroform) was spin coated onto the perovskite layer at 4000 rpm (ramp: 4000 rpm/s) for 60 s without annealing. A 70 $\mu{\rm L}$ drop of BCP solution (0.5 mg/mL in 2-propanol) was spin coated onto the PC $_{60}$ BM layer at 4000 rpm (ramp: 4000 rpm/s) for 60 s without annealing. The devices were finished by the deposition of a 150 nm Ag layer at the rate of 0.2 nm/s with a mask to a final device size of 0.0314 cm². The thermal evaporation processes were performed in a background vacuum less than 2×10^{-6} Torr.

Device Characterization. The photocurrent density-voltage (J-V) measurements were performed in a N_2 filled glovebox and recorded by a Keithley 2400 source meter from -0.5 to 1.5 V (forward scan) or 1.5 V to -0.5 V (reverse scan) under illumination by a 450 W oriel xenon lamp with a AM 1.5G filter solar simulator (100 mW/cm^2). The light intensity was calibrated with a standard Si photodiode equipped with KG-5 filter. The calibration diode was calibrated by the National Renewable Energy Laboratory. The EQE spectra were measured using a setup consisting of a xenon lamp (Oriel, 300 W) as a light source, a monochromator (Newport Cornerstone 130), a mechanical chopper (Stanford Research Systems Inc.) with a frequency of 200 Hz, a lock-in amplifier (Stanford Research Corp SR830), and a NIST-certified Si photodiode (Thorlabs FDS 100-CAL) for calibration. The

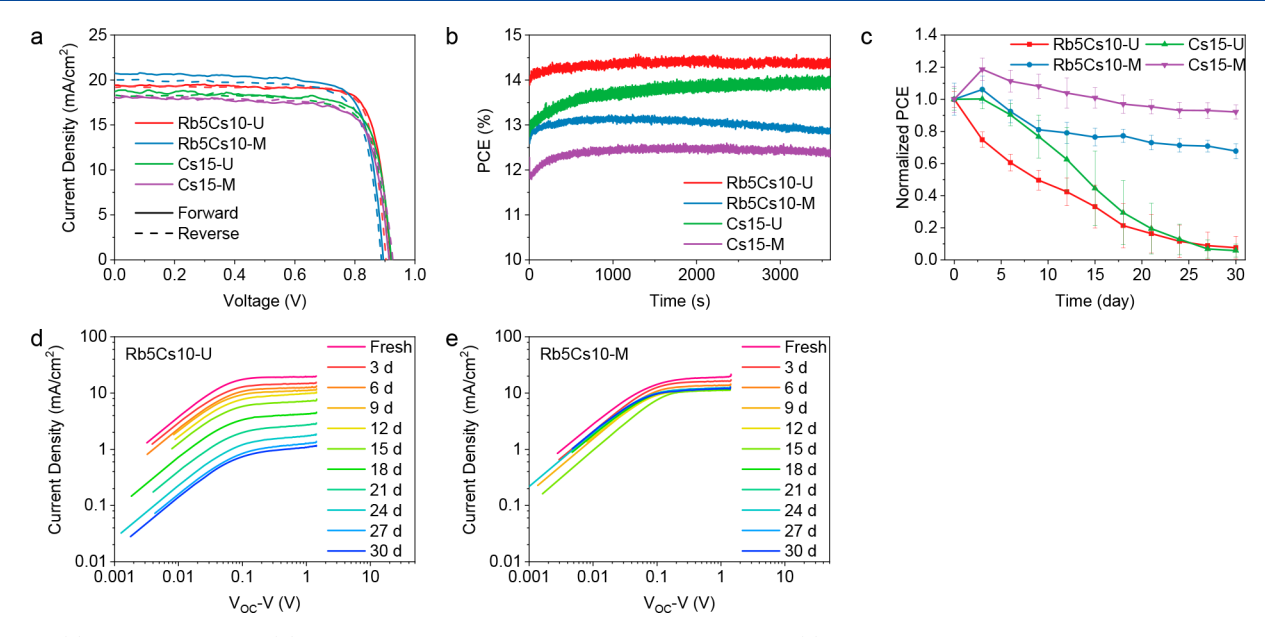


Figure 1. (a) J-V characteristics, (b) PCE versus time at the maximum power output, and (c) normalized PCE versus time for the solar cells based on Rb5Cs10-U, Rb5Cs10-M, Cs15-U, and Cs15-M perovskite active layers. (d, e) Photocurrent density versus effective voltage of the solar cells with Rb5Cs10-U and Rb5Cs10-M active layers, respectively, by tracking the same device over 30 days.

Table 1. Average Photovoltaic Parameters of the Perovskite Solar Cells Based on Different Active Layers

active layer	$J_{\rm sc}~({\rm mA/cm}^2)$	$V_{\rm oc}$ (V)	FF	PCE (%)
Rb5Cs10-U	17.65 ± 0.72	0.93 ± 0.01	0.81 ± 0.01	13.22 ± 0.52
Rb5Cs10-M	17.00 ± 1.10	0.92 ± 0.02	0.74 ± 0.02	11.52 ± 1.10
Cs15-U	18.16 ± 0.70	0.91 ± 0.01	0.74 ± 0.02	12.17 ± 0.84
Cs15-M	15.04 ± 0.84	0.90 ± 0.02	0.67 ± 0.03	9.05 ± 0.68

EQE spectra were integrated over AM 1.5G photon flux to attain photocurrent density.

■ RESULTS AND DISCUSSIONS

One-step solution process of hot casting with antisolvent was applied to fabricate $Rb_{0.05}Cs_{0.10}FA_{0.85}PbI_3$ and $Cs_{0.15}FA_{0.85}PbI_3$ perovskite thin films, ² which are named as Rb5Cs10 and Cs15, respectively. The perovskite films prepared using well-mixed precursor solutions denoted as Rb5Cs10-M or Cs15-M while those without stirring as Rb5Cs10-U or Cs15-U. The perovskite solar cells were fabricated in an inverted structure as $ITO/PEDOT:PSS/Perovskite/PC_{60}BM/BCP/Ag$, where perovskite active layers are Rb5Cs10-M, Rb5Cs10-U, Cs15-M, and Cs15-U, respectively.

Figure 1a shows the current density-voltage (J-V)characteristics of the devices under forward and reversed scans, and the device performance parameters are summarized in Table 1. All devices show ignorable hysteresis. Devices fabricated with unmixed precursor solutions exhibit better performance than their counterparts with well-mixed precursor solutions. Rb5Cs10-U devices show a J_{SC} of 17.65 mA/cm², a $V_{\rm OC}$ of 0.93 V, an FF of 0.81, and a PCE of 13.22%. The Rb5Cs10-M devices give a slightly reduced J_{SC} of 17.00 mA/ cm² and $V_{\rm OC}$ of 0.92 V, while a heavily reduced FF of 0.74, which results in a reduced PCE of 11.52%. The Cs15-U and Cs15-M devices show a similar trend, with $J_{\rm SC}$ reduced from 18.16 to 15.04 mA/cm², $V_{\rm OC}$ from 0.91 to 0.90 V, FF from 0.74 to 0.67, and in sum, PCE from 12.17 to 9.05%. The EQE spectrum (Figure S1 of the Supporting Information, SI) of the Rb5Cs10-M device shows a sharp cutoff around 830 nm and

an integrated photocurrent density of 17.30 mA/cm². The incorporation of Rb⁺ cation boosts up the device performance regardless of well-mixed or unmixed precursor solutions. All devices exhibit a good short-term stability at the maximum power output (MPP) over 1 h measurement.

The long-term device stability was evaluated by measuring the I-V curves every 3 days for 30 days. The devices were stored in a N₂ glovebox without encapsulation in dark between measurements. As shown in Figure 1c, the PCEs of both Cs15-U and Rb5Cs10-U devices drop significantly to less than 10% of the initial values over the 30 days testing period. The Cs15-U devices show a relatively improved stability in the first 20 days than the Rb5Cs10-U devices. The Cs15-M devices exhibit even increased PCEs in the first 15 days with a peak PCE about 20% higher than the initial values on the third day. The PCEs retain 92% of the initial values at the end of 30 days. The Rb5Cs10-M devices also exhibit an initial PCE increase in the first 3 days but a quick drop of PCE in the next 6 days and then maintain 68% of the PCEs to the end of 30 days. The losses of PCEs are mainly due to the decrease of J_{SC} 's as the $V_{\rm OC}$'s remain unchanged over the 30 days for all devices and the FFs even increase for the Rb5Cs10-M and Cs15-M devices (Figure S2a-c).

The reduction of $J_{\rm SC}$ is generally attributed to interfacial degradation and/or active layer degradation, which mainly affect the charge carrier extraction rate^{29–31} and the charge carrier generation and transport rate,³² respectively. We plotted the photocurrent density versus effective voltage for Rb5Cs10-U and Rb5Cs10-M devices by racking the same devices in a 3-day interval for 30 days (Figure 1d,e). The photocurrent densities reach the plateaus at a low effective

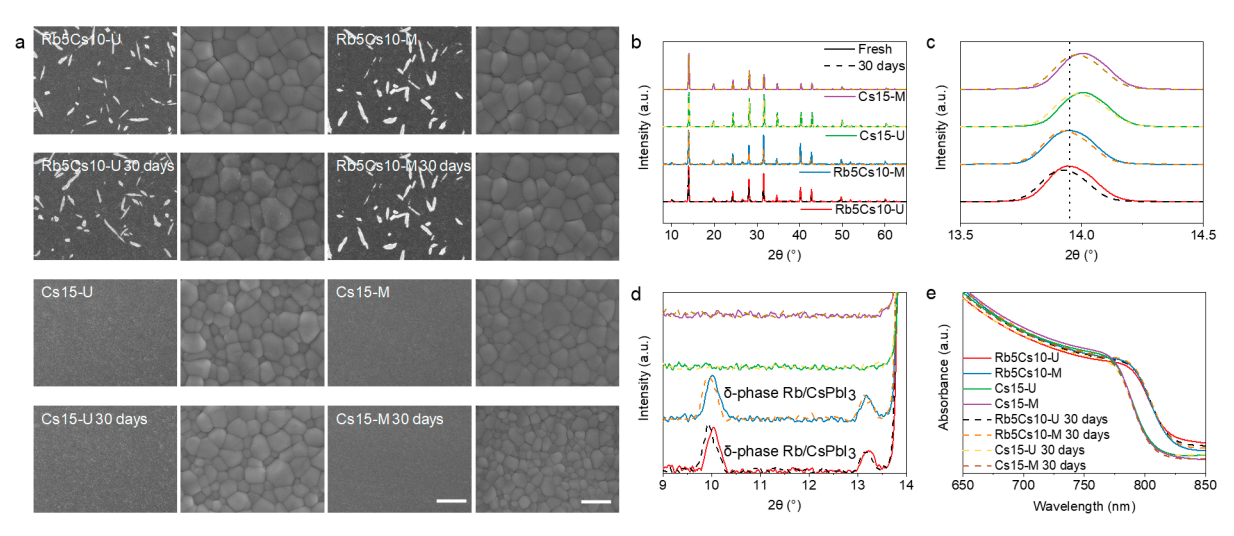


Figure 2. (a) SEM images, (b-d) XRD patterns, and (e) UV-vis absorption spectra of Rb5Cs10-U and Rb5Cs10-M, and Cs15-U and Rb5Cs10-M thin films on glass/PEDOT:PSS substrates that are freshly prepared and after stored in dark under N_2 protection for 30 days. Scale bars are 5 μ m and 500 nm for the low and high magnification images, respectively.

voltage of 0.1-0.2 V, suggesting that charge carriers are swept out efficiently and interfacial charge extraction is not a limiting factor of the device performance.³³ In addition, the plateau effective voltage, at which the photocurrent densities reach the plateaus, does not change over the storage time, indicating that the reduction of J_{SC} is not caused by the interfacial degradation. The Rb5Cs10-U device exhibits a decreased plateau current density at high effective voltage over the 30 days testing, indicating that the charge carrier generation rate in the active layer is the reason for the device degradation. In contrast, the plateau current density of the Rb5Cs10-M device decreases in the first 9 days and then maintains almost the same in the following 21 days, suggesting that the charge generation rate is maintained at the similar level. Similarly, both Cs15-U and Cs15-M devices exhibit the constant plateau effective voltage of 0.1-0.2 V over the 30 days, while the plateau current density of Cs15-U significantly decreases and that of Cs15-M remains constant (Figure S2d,e). The decreased plateau current density again indicates the reduced charge generation rate in the active layer.

To fully understand the impacts of mixed Rb⁺ and Cs⁺ cation versus single Cs+ cation doping in the A-site of FAPbI₃ as well as the precursor preparation methods on MA-free device performance and stability, we characterized freshly made and aged thin films as well as the active layers after device stability tests. SEM images (Figure 2a), XRD patterns (Figure 2b-d), and UV-vis spectra (Figure 2e) show that there are no significant differences in film morphology, crystalline phase, and optical band gap for Rb5Cs10-U and Rb5Cs10-M films or Cs15-U and Cs15-M films. However, differences are observed for perovskites with or without Rb. White rods present on both Rb5Cs10-U and Rb5Cs10-M films but not on Cs15-U and Cs15-M films (Figure 2a). The energy dispersive spectroscopy (EDS) of the Rb5Cs10-U thin film shows the white rod regions have higher amount of Cs and Rb, especially Rb, while less FA content (indicated by element N) compared to these element contents in the background regions (Figure S3 and Table S1). Giving the same total 15% substitutional quantity of small cations for FA cations and the smaller radius of Rb+ (1.52 Å) than Cs+ (1.67 Å), the (110) peak of a Rb5Cs10 thin film should appear at the higher diffraction angle than that of a Cs15 thin film if all small

cations are integrated into the perovskite lattice. However, Figure 2c shows that the (110) peaks of the Rb5Cs10 thin films are at 13.94° compared to 14.00° for the Cs15 thin films, indicating that less Cs+ and Rb+ cations are integrated into the perovskite lattices.¹¹ In addition, two extra peaks, corresponding to the δ -phase Rb/CsPbI₃, 18,20,24,34,35 present at 10.04° and 13.22° for the Rb5Cs10-U thin film and at 10.02° and 13.18° for the Rb5Cs10-M thin film (Figure 2d). The EDS and XRD results indicate that the white rods could be enriched δ -phase Rb/CsPbI₃ segregated from the Rb5Cs10 perovskites. The UV-vis spectra show that the absorption cutoffs of Rb5Cs10 perovskite thin films are around 832 nm, exhibiting an obvious red shift comparing with the cutoffs around 821 nm for Cs15 thin films, which is attributed to the less incorporation of small Cs⁺ and Rb⁺ cations in the perovskite lattice. ^{20,36} The SEM, EDS, XRD, and UV-vis results reveal that Rb⁺ cation is less effectively integrated into the FAPbI₃ lattice than Cs⁺ cation and codoping Rb⁺ with Cs⁺ could even induce the segregation of Cs⁺ cation along with Rb⁺ cation, forming mixed δ -phase Rb/CsPbI₃ white rods on the Rb5Cs10 films.

To rule out the effect of mixed Rb⁺ and Cs⁺ cation doping and single Cs+ cation doping on FAPbI3 perovskite phase stability, we conducted SEM, XRD, and UV-vis s experiments after storing all four thin films under N2 protection in dark for 30 days. SEM images show white crumbs present on the aged Rb5Cs10-U perovskite grains, which is similar to the feature reported previously,²⁰ while no obvious morphology changes for the other three films. XRD patterns show a 0.02° downshift of the (110) peak for all films, indicating a slight segregation of small cations upon storage. In addition, the peak corresponding to the δ-phase Rb/CsPbI₃ also shifts from 10.04° to 9.92° and from 10.02° to 9.94° for the Rb5Cs10-U and Rb5Cs10-M film, respectively, indicating that more Cs⁺ cations segregate out of the Rb5Cs10-U film than the Rb5Cs10-M film because the lattice parameter of CsPbI₃ is larger than RbPbI₃. There are no obvious differences at the absorption edges for all thin films after storage (Figure 2e). The aging results indicate that single Cs⁺ cation doped Cs15 perovskites are stable regardless how the precursor solutions were prepared. In contrast, the phase stability of mixed Rb+ and Cs⁺ cation doped Rb5Cs10 perovskites is influenced by the means that the precursor solutions were prepared. A well-

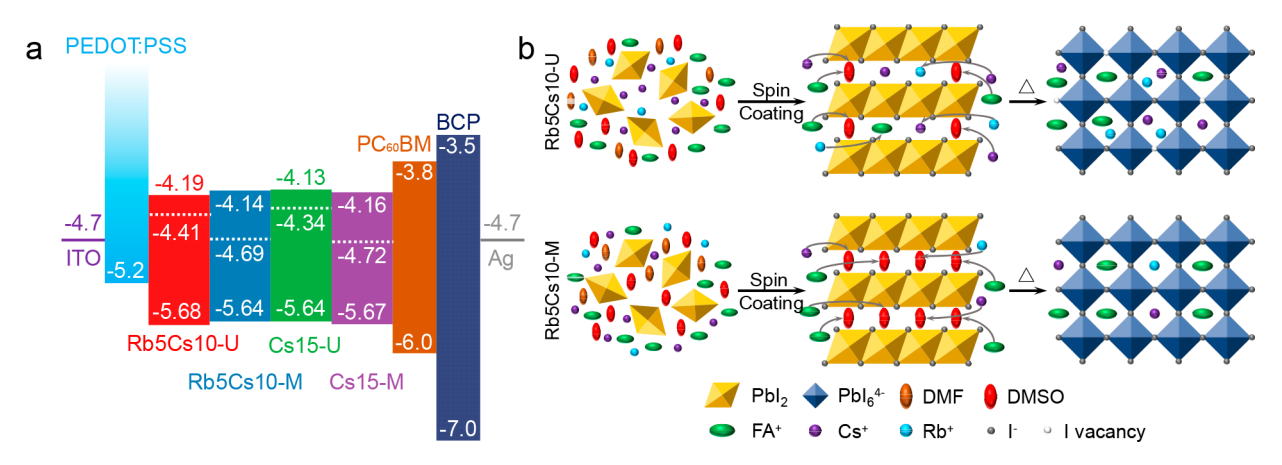


Figure 3. (a) Energy level diagram of the materials in the inverted structured perovskite solar cells. The valence band maxima (VBM) and Fermi levels (dotted lines) of all perovskite films were obtained from UPS while the conduction band minima (CBM) were estimated by adding the VBM and optical band gaps obtained from the UV—vis absorption spectra. (b) Schematic illustration of unmixed and mixed precursor solutions resulting in the A-site interstitial defects in the Rb5Cs10-U film but less defects in the Rb5Cs10-M film.

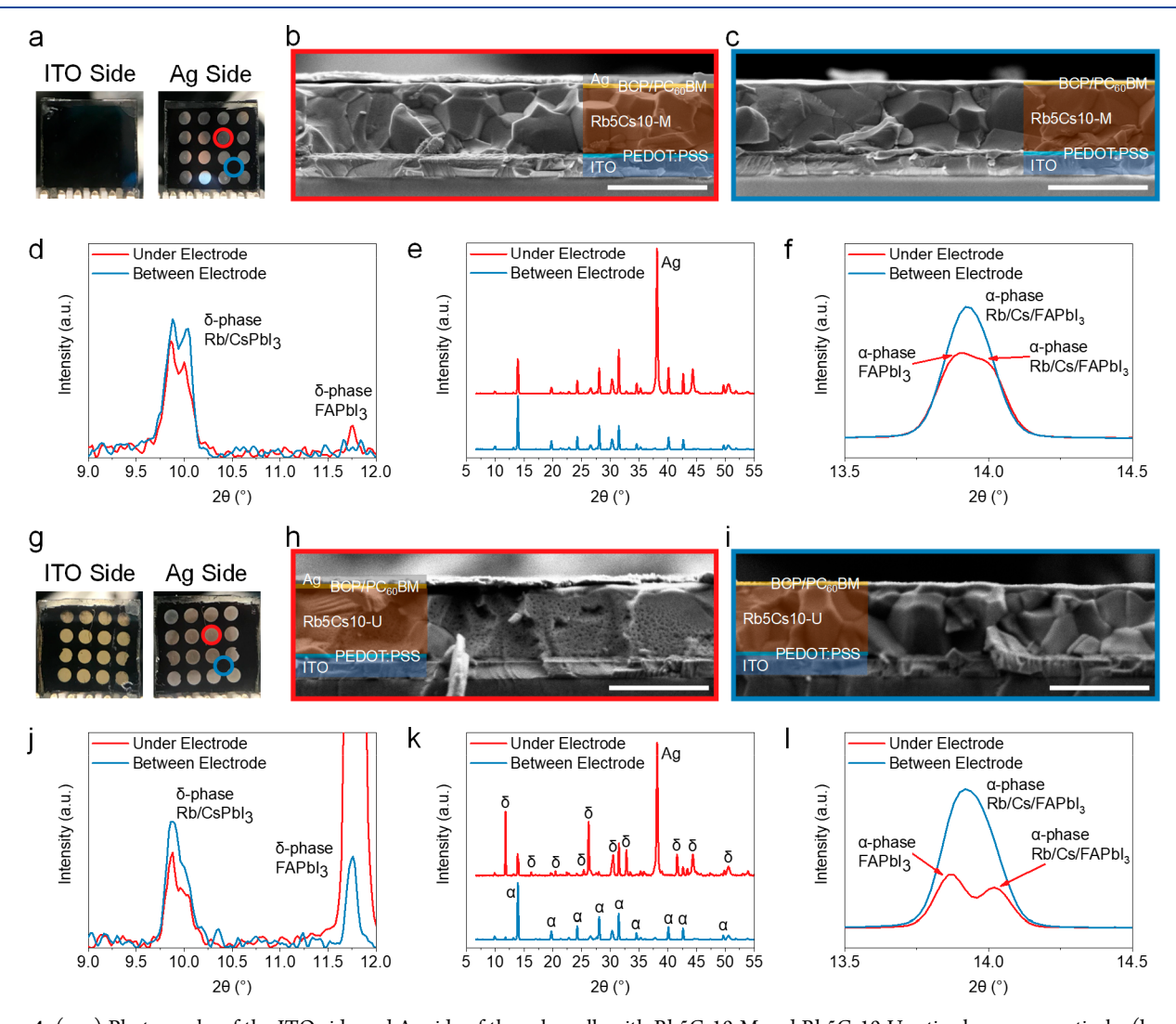


Figure 4. (a, g) Photographs of the ITO side and Ag side of the solar cells with Rb5Cs10-M and Rb5Cs10-U active layers, respectively. (b, c, h, i) Cross-sectional SEM images of the solar cells with Rb5Cs10-M and Rb5Cs10-U active layers in the areas between Ag electrodes (blue circles and blue frames) and under Ag electrodes (red circles and red frames). (d-f, j-l) XRD patterns taken from the areas between Ag electrodes and under electrodes of the solar cells with Rb5Cs10-M and Rb5Cs10-U active layers. The devices are those that have been tested in a 3-day interval for 30 days.

mixed precursor solution leads to a more stable Rb5Cs10 perovskite while an unmixed precursor solution results in more segregation of small cations.

We investigated the band structures of these four perovskites using ultraviolet photoelectron spectroscopy (UPS) (Figure S4) and determined their valence band maxima (VBM) and Fermi levels (Table S2). The conduction band minima (CBM) were calculated by adding the optical band gaps to the VBM. Figure 3a shows the derived energy level diagram of four perovskite films along with the transport layer and electrode materials. Both Rb5Cs10-U and Cs15-U perovskites show a strong n-type semiconductor feature with the Fermi levels 0.52 and 0.54 eV above the middle band gap, respectively, while both Rb5Cs10-M and Cs15-M perovskites show a weak n-type feature with the Fermi levels 0.2 eV above the middle band gap. Previous studies of MAPbI3 perovskite show that Ivacancy (V₁), MA⁺ and Pb²⁺ interstitial sites (MA_i and Pb_i), cation substitution (Pb_{MA}), and antisite substitution (MA_I and Pb₁) can cause n-type doping.³⁷ Except the interstitial site Pb₁ and antisite substitution Pb_I causing deep level traps, all others make shallow level traps and the formation energy of these point defects is low. Experiments have demonstrated that MAPbI₃ can be tuned from p-type to n-type by adjusting the MAI and PbI₂ concentration ratio or creating Pb²⁺ rich and MA+ and I- deficiency through thermal annealing to remove MAI.³⁸ MAPbI₃ was heavily n-doped with a high electron concentration of 2.8×10^{17} cm⁻³ even with the stoichiometric ratio. At room temperature, the MA⁺ interstitial defect has the highest concentration of 1×10^{12} cm⁻³ and the I⁻ vacant defect concentration is about 5 orders of magnitude lower.³¹ The n-type doping level difference of our perovskite films could be related to the formation of point defects in making Rb5Cs10-U and Cs15-U perovskite films and Rb5Cs10-M and Cs15-M perovskite films because the only difference is that the precursor solutions were magnetically stirred or not prior to spin coating. As illustrated in Figure 3b, in the unmixed precursor solution, PbI₂ octahedrons are most surrounded by Rb⁺ and Cs⁺ cations due to their high affinity to PbI₂. In contrast, in the well-mixed precursor solution, PbI2 octahedrons are surrounded by more homogeneously distributed DMSO and DMF solvent molecules. The PbI₂-DMSO intermediates were formed after the antisolvent DEE washes off the majority of DMSO and DMF solvent molecules and the perovskite structure with corner-sharing octahedrons was formed by extracting DMSO molecules and diffusion of Asite cations during thermal annealing. 40,41 For Rb5Cs10-U and Cs15-U samples, Rb⁺ and Cs⁺ cations have partially filled the spaces between the PbI₂-DMSO intermediates, and some Rb⁺ and Cs⁺ cations are trapped in the interstitial A-sites after annealing, resulting in more defects and strong n-type perovskites. For Rb5Cs10-M and Cs15-M samples, DMSO molecules slow down the interdiffusion process and crystallization, resulting in less defects, and thus weak n-doping. The UPS results reveal that both Rb5Cs10-U and Cs15-U perovskites are stronger n-doped than Rb5Cs10-M and Cs15-M perovskites, which could be attributed to more Asite interstitials in perovskite films made by unmixed precursor solutions. The heavily n-doping and possible higher electron concentration in Rb5Cs10-U and Cs15-U perovskites yield the better device performance, especially larger J_{sc}'s for Rb5Cs10-U and Cs15-U devices (Figure 1a and Table 1).

Since codoping Rb⁺ with Cs⁺ induced more phase segregation and PCE decrease over time, we further

characterized the perovskite active layers after the Rb5Cs10-M and Rb5Cs10-U devices have been tested in a 3-day interval for 30 days. Figure 4a shows the photographs of the front-side (Ag electrode) and back-side (glass/ITO) of the Rb5Cs10-M devices after 30 days testing. The back-side photograph shows black color in the entire active layer film, indicating that Rb5Cs10-M perovskite is photoactive α -phase. We took the cross-sectional SEM images specifically in the areas under an Ag electrode (Figure 4b) and between Ag electrodes (Figure 4c). The SEM images show that the Rb5Cs10-M perovskite thin films have a thickness of approximately 700 nm with nice polycrystalline structures and clear grain boundaries in both areas. We also acquired the XRD patterns in these two areas (Figures 4d-f). There are no obvious differences in the overall XRD patterns except some peak intensity changes and an Ag diffraction peak centered at 38.12° in the XRD pattern taken under the Ag electrode (Figure 4e). However, some changes are observed in the zoom-in low angle region and the (110) peak. Figure 4d shows a tiny δ -phase FAPbI₃ peak centered at 11.76° in the XRD pattern taken under the Ag electrode but not present between electrodes. Figure 4f shows that the (110) peak in the XRD pattern taken from the area between electrodes still maintains a single peak of α -phase, while it slightly splits into two peaks collected under the electrode with one peak corresponding to FAPbI3-rich phase while another corresponding to more Rb⁺ and Cs⁺ in FAPbI₃. Even the single peak from the area between electrodes also shifts slightly to the low angle centered at 13.92° compared to 13.94° for the film that has been stored in a N2 glovebox for 30 days (Figure 2c). The XRD results indicate that phase segregation occurs in the Rb5Cs10-M active layer, especially under the Ag electrode during the course of device testing. The emerging δ -phase FAPbI₃ in the active layer under the Ag electrode could be due to the phase transition of small clusters of pure α -phase FAPbI₃ that are formed in the Rb5Cs10-M film.

A dramatically visual difference is shown by photographs in Figure 4g. Devices containing the Rb5Cs10-U active layer show a see-through photograph taken from the glass/ITO side after 30 days testing. The Rb5Cs10-U active layer turns to yellow under the Ag electrodes, making the electrodes visible from the back-side. However, the Rb5Cs10-U active layer between electrodes remains black. The cross-sectional SEM image taken under the electrode shows pinholes in grains and blurry grain boundaries (Figure 4h), in comparison to dense grains and clear grain boundaries exhibited in the SEM image between Ag electrodes (Figure 4i). The overall XRD patterns in Figure 4k show the coexistence of photoactive α -phase and photoinactive δ -phase perovskites in the active layer under the electrode, while mainly photoactive α -phase perovskite in the active layer between electrodes. Much stronger δ -phase FAPbI₃ peak at 11.76° exhibits in the active layer under the electrode than between electrodes (Figure 4j). The α -phase (110) peak of the Rb5Cs10-U active layer under the electrode splits into two peaks, centered at 13.86° and 14.02° (Figure 41), corresponding to pure α -phase FAPbI₃ and the α -phase FAPbI₃ with highly incorporated Rb⁺ and Cs⁺ cations. ⁴² The content of Rb⁺ and Cs⁺ cations is even higher than the freshly made films because the (110) peak is shifted to 14.02° compared to the location at 13.94°. The SEM images and XRD patterns indicate a material loss and phase segregation in the Rb5Cs10-U active layer under the electrode. The relatively pure α -phase FAPbI₃ small crystals transferred to the yellow photoinactive δ -phase under the electrode over time.

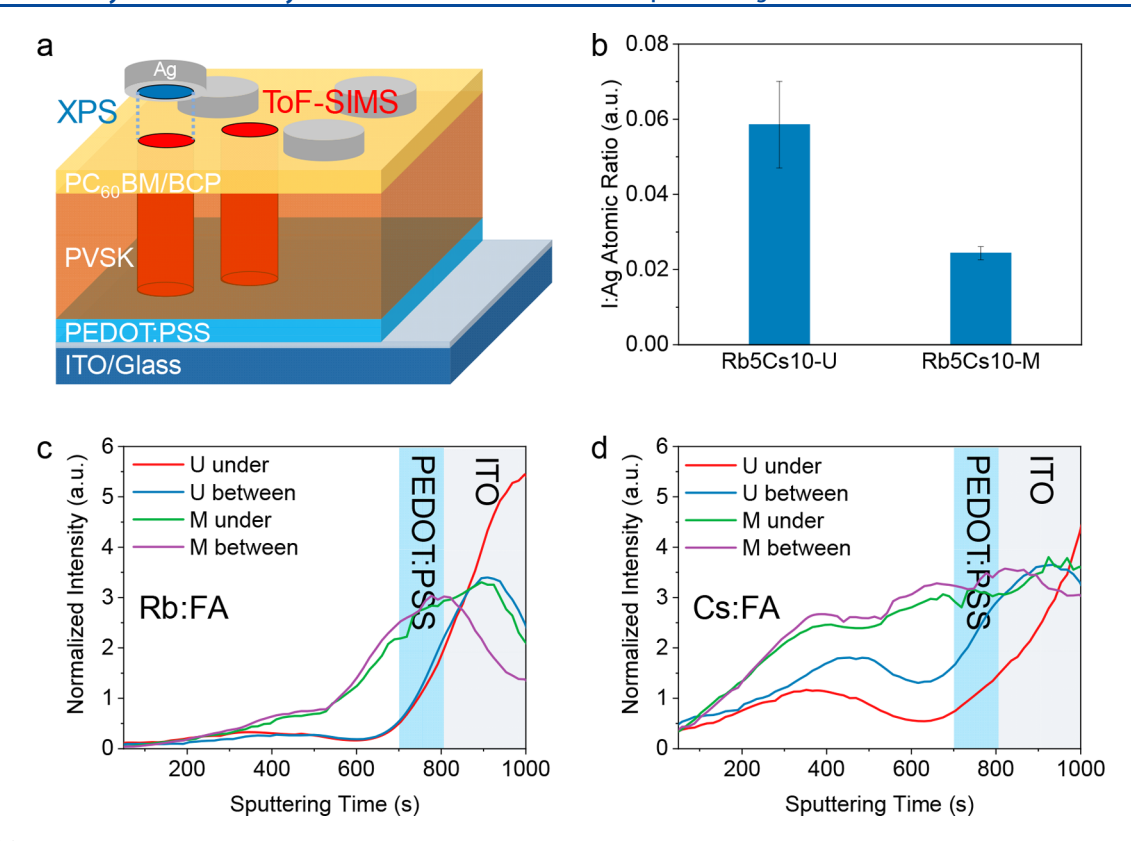


Figure 5. (a) Schematic illustration of the regions where XPS and ToF-SIMS experiments were performed indicated by blue and red, respectively. (b) Atomic ratio of I to Ag determined by XPS measured at the peel-off Ag electrodes from the Rb5Cs10-M and Rb5Cs10-U devices after testing for 30 days. (c) The Rb to FA and (d) Cs to FA content ratio profiles determined by ToF-SIMS for the Rb5Cs10-M and Rb5Cs10-U devices in the regions between electrodes and under the electrode.

Apparently, ions must migrate in this process. The Cs15-M and Cs15-U devices show the similar visual pictures as the Rb5Cs10-M and Rb5Cs10-U devices after testing for 30 days, and their XRD patterns are shown in Figure S5 and discussed in the SI.

To find the evidence of ion migration, we first characterized the chemical components of the Ag electrodes at the side touching the electron transport layer (ETL). The Ag electrodes were carefully peeled off and the survey and highresolution XPS scans (Figure S6) were taken at the Ag electrode side contacting the ETL as illustrated in Figure 5a. The survey scans (Figure S6a,d) show iodine signal on the Ag electrode but no Rb and Cs signals. The core level spectra of I 3d and Ag 3d (Figures S6b,c,e,f) show the binding energy of 619.2 and 368.2 eV for I $3d_{5/2}$ and Ag $3d_{5/2}$, respectively, corresponding to I⁻ in AgI compound and Ag⁺ in the hybrid of AgI and Ag. 43 The I:Ag atomic ratios on the Ag electrodes were calculated by integrating the peak areas of Ag 3d and I 3d in the survey scans. More than the twice of the I:Ag atomic ratio was found on the Ag electrode from the Rb5Cs10-U device compared to the Rb5Cs10-M device (Figure 5b). Forming AgI in the Ag electrode due to iodide ion migration have been reported in previous studies. 43-45 The higher I:Ag atomic ratio on the Ag electrode from the Rb5Cs10-U device and the strong n-type doping of Rb5Cs10-U films shown by the UPS results demonstrate that more halide vacancies exist in the Rb5Cs10-U film than in the Rb5Cs10-M film. We further used ToF-SIMS to characterize the elemental depth profiles in the regions under the electrode and between electrodes for both Rb5Cs10-U and Rb5Cs10-M devices (Figure S8). The Rb:FA and Cs:FA cation ratio profiles are shown in Figure

5c,d, respectively. Clearly, Rb+ cations show a strong diffusion direction toward the PEDOT:PSS and ITO layers. The Rb content in the Rb5Cs10-U active layer is less than that in the Rb5Cs10-M active layer because more Rb+ cations have diffused into the PEDOT:PSS and ITO layers. For both Rb5Cs10-U and Rb5Cs10-M active layers, more Rb present in the PEDOT:PSS and ITO layers in the region under the electrodes. Similarly, Cs⁺ cations also diffuse toward the PEDOT:PSS and ITO layers, leaving a Cs depletion zone in the active layer close to the ETLs. The Rb5Cs10-U active layer has a lower Cs content than the Rb5Cs10-M active layer. The Cs content is lower in the regions under the electrodes, especially for the Rb5Cs10-U active layer. The XPS and ToF-SIMS results show that after testing the devices in a 3-day interval for 30 days, iodide anions present in the Ag electrodes while Rb⁺ and Cs⁺ cations in the PEODT:PSS and ITO layers, the consequence of anion and cation migration in the opposite directions. The applied external electric field accelerates these ion migrations and the active layer, prepared with the unmixed precursor solutions, exhibit more serious Rb⁺ and Cs⁺ cation and I⁻ anion deficiency in the active layer.

The comprehensive characterizations of both stand-alone perovskite films and the perovskite active layers in the inverted structured devices allow us to understand the device performance and the stability related to the mixed Rb^+ and Cs^+ and single Cs^+ cation doping as well as the precursor solution preparation methods induced defects in $Rb_{0.05}Cs_{0.10}FA_{0.85}PbI_3$ and $Cs_{0.15}FA_{0.85}PbI_3$ perovskites. The device performances were significantly improved by replacing 5% of Cs^+ cation in $Cs_{0.15}FA_{0.85}PbI_3$ with Rb^+ forming $Rb_{0.05}Cs_{0.10}FA_{0.85}PbI_3$, even though Rb^+ cations were not

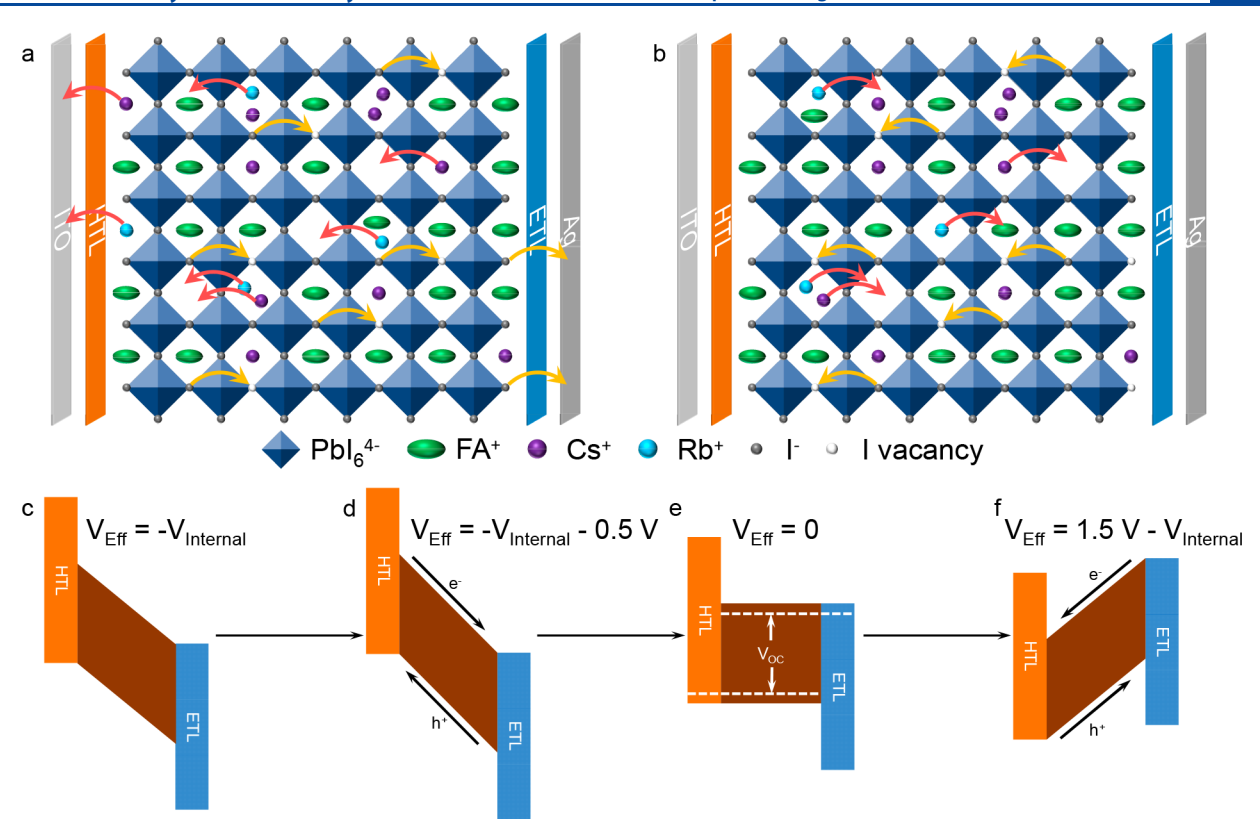


Figure 6. Schematic illustration of ion migration in the perovskite film under (a) negative effective electric field and (b) positive electric field. Effective electric field applied on the perovskite active layer following the testing sequence: (c) under dark without external bias, and under illumination with (d) -0.5 V reverse external bias, (e) V_{oc} forward external bias, and (f) +1.5 V forward external bias.

completely integrated into the perovskite lattice and Rb/ CsPbI₃ phase was observed on the perovskite surface. The improved device performance of Rb_{0.05}Cs_{0.10}FA_{0.85}PbI₃ than Cs_{0.15}FA_{0.85}PbI₃ was also observed in the conventional structured devices and the white segregation of Rb/CsPbI₃ phase presented on the Rb_{0.05}Cs_{0.10}FA_{0.85}PbI₃ thin film.²⁰ The difficulty to integrate Rb+ cation into perovskites lattices has been reported in a variety perovskites from MAPbI₃, FAPbI₃, and MA/FAPbI $_3$ to MA/FAPb(I/Br) $_3$ with single Rb $^+$ cation or mixed Rb $^+$ and Cs $^+$ cation. Nonetheless, even a small amount of Rb+ integration can increase charge carrier mobility and slow down charge recombination, 18,46,47 which could also be the underline factors improving the device performance of our Rb5Cs10-M and Rb5Cs10-U devices. The better device performance of the Rb5Cs10-U and Cs15-U devices than the Rb5Cs10-M and Cs15-M devices benefits from the heavily n-doping of these perovskites, which increases electron carrier concentration, improves the charge carrier transport, and eventually enhances the $J_{\rm SC}$ and FF.³⁸ It has also been reported that the benign defects in the perovskite could improve the performance by aggregating at the perovskite/ transport layer interface and heal the deep defects, therefore, improve the charge carrier collection.⁴⁹

Even though both Rb⁺ cation incorporation and benign defects in the perovskites make the positive impacts on the initial device performance, they cause the long-term instability of the devices due to ion migration under electric field. The n-type doping nature of these perovskites means the presence of many types of point defects, particularly, halide vacancies and A-site cation interstitial sites as illustrated in Figure 6a,b. Other types of defect such as A-site vacancy and grain boundary

defects may also exist in the perovskite and serve as the cation migration channels. The effective voltage $(V_{
m eff})$ is the actual voltage applied to the active layer involving both built-in internal electric field and applied external voltage. When the device is in the dark with no applied external voltage, the active layer experienced a built-in internal field (Figure 6c). When we conducted the stability test in a 3-day interval for 30 days, the devices were always swapped from -0.5 to 1.5 V. The effective voltage is even stronger under an applied reverse external bias (-0.5 to <0 V, Figure 6d). In both cases, as illustrated in Figure 6a, I anions move toward the Ag electrode side mediated by the halide vacancies, and interstitial (even some A-site) small Cs+, and especially Rb+ cations migrate toward the ITO electrode side via different path ways,²⁸ while large FA+ cations mainly remain in their positions because of the hydrogen bonding with iodide atoms. When the applied external voltage is equal to $V_{\rm oc}$, the effective voltage is equal to zero, no ion migrations occurs but this is a very short period. When the device is under a forward external bias (0-1.5 V,Figure 6f), the effective voltage applied to the active layer is reversed. Consequently, Rb+ and Cs+ cations and I- anions migrate in the opposite directions as illustrated in Figure 6b. Since the devices were stored in the dark during the course of 30 days testing, the active layers were experienced a constant built-in voltage, which drives the slow migration of Rb+ and Cs⁺ cations toward the ITO electrode side and I⁻ anions toward the Ag electrode side and they even diffuse through the transport layers and are permanently captured in electrodes. Therefore, after 30 days device testing, the iodide element is testable in the Ag electrode by XPS and enriched Rb and Cs elements in the ITO side shown by ToF-SIMS. In contrast, in

the conventional structured devices, the migrated cations and anions accumulate at the HTL/perovskite and ETL/perovskite interfaces. Under illumination and open circuit voltage, light induced self-pooling makes ions redistribution in the active layer, which has been attributed to the origin of hysteresis.⁵⁰ The losses of materials in the active layer under dark and reverse applied external voltage create more defects, which facilitates ion migration under the applied higher forward external bias. Consequently, small clusters with relative pure α phase FAPbI₃ are formed in the active layer, which are easily transferred to the thermodynamically more stable δ -phase FAPbI₂ under room temperature. To further confirm our hypothesis regarding the effect of electric field on the device stability, we also performed the stability test on the Rb5Cs10-U device with longer testing intervals, 15 days and 30 days (Figure S7). The PCEs at the 30 days retain 20% and over 40% of the initial PCEs for the devices tested in a 15-day and 30day interval, respectively, while the PCE is below 10% of the initial PCE for the devices tested in a 3-day interval. The reduced PCEs are again mainly due to the decrease of J_{SC} 's. These results confirm that the electric field plays a crucial role in the ion migration process. The better PCEs after 30 days for the devices tested in longer intervals might also be due to the less light exposure. The reduction of PCEs for longer testing intervals, especially the interval of 30 days, indicates that the built-in internal electric field can cause ion migrations. In the inverted structured devices, the migrated small inorganic cations and halide anions are captured in electrodes, creating more defects in perovskite. A frequently applied electric field accelerates phase segregation, creating small clusters of pure α phase FAPbI₃, which transfers to photoinactive δ -phase FAPbI₃ under room temperature, and finally resulting in the degradation of device. We should point out that the reported long-term device stability based on MA-free Rb_{0.05}Cs_{0.10}FA_{0.85}PbI₃ perovskite was achieved in the conventional structured device and the device was tracking under continuous maximum power point, at which the applied voltage is close to $V_{\rm oc}$ and thus, ion migration is physically suppressed.²⁰ The further improved stability by applying PMMA in both HTL/perovskite and ETL/perovskite interfaces could be due to the mitigation of ion diffusion into transport layers.

CONCLUSIONS

In summary, we prepared two types of MA-free perovskite, Rb_{0.05}Cs_{0.10}FA_{0.85}PbI₃ and Cs_{0.15}FA_{0.85}PbI₃, and investigated the effect of Rb+ on the device performance and long-term device stability against electric field. We demonstrated that the incorporation of Rb+ cation in the perovskite lattice was incomplete, but it improved the device performance even though reduced the long-term device stability. We revealed that the degradation of the inverted structured devices was due to phase segregation caused by ion migration under electric field and the losses of I- anions and Rb+ and Cs+ cations captured by the electrodes. We showed that by stirring the precursor solution prior to spin coating, the defect density in the perovskite was significantly reduced and the device longterm stability was improved. The stabilized Rb_{0.05}Cs_{0.10}FA_{0.85}PbI₃ and Cs_{0.15}FA_{0.85}PbI₃ devices retained 68% and 92% of the initial PCE, respectively, after 30 days under N₂ protection. Our work elucidates that codoping Rb⁺ with Cs⁺ cation is still promising for FAPbI₃ but ion migration under electric field needs to be suppressed. Our work also

reveals that mixing precursor solution prior to spin coating is one of the accessible methods to reduce the defect densities, therefore the ion migration in the perovskite solar cells. Our work sheds light on the solution of the operational instability of perovskite solar cells and paves the pathway for their industrialization.

ASSOCIATED CONTENT

Supporting Information

The Supporting Information is available free of charge at https://pubs.acs.org/doi/10.1021/acs.jpcc.0c05357.

EQE spectrum and the integrated current density of the Rb5Cs10-M device; normalized $V_{\rm OC}$, FF, and $J_{\rm SC}$ of the solar cells with Rb5Cs10-U, Rb5Cs10-M, Cs15-U, and Cs15-M active layers stored in a N2 filled glovebox in dark at room temperature with a testing interval of 3 days for 30 days; photocurrent density versus effective voltage of the solar cells with Cs15-U and Cs15-M active layers by tracking the same device over 30 days; SEM image of Rb5Cs10-U perovskite thin film; EDS data collected from the thin film background and while rod region along with the corresponding element molar percentage in the Rb5Cs10-U perovskite thin film; UPS spectra of Rb5Cs10-U and Rb5Cs10-M, and Cs15-U and Cs15-M thin films; work function, valence band maximum, optical band gap, and conduction band minimum of four MA-free perovskites; XRD patterns taken from the areas between Ag electrodes and under the electrode of the solar cells with Cs15-M and Cs15-U active layers; survey and high-resolution Ag 3d and I 3d XPS spectra of Rb5Cs10-U and Rb5Cs10-M; normalized ToF-SIMS profiles of Rb, Cs, FA, Pb, and Na elements acquired from the areas under the electrodes and between electrodes of the solar cells tested for 30 days with Rb5Cs10-U and Rb5Cs10-M active layers; and normalized PCE, J_{SC} , V_{OC} , and FF of solar cells with a Rb5Cs10-U active layer stored in N2 filled glovebox under room temperature for 30 days with the testing intervals of 3, 15, and 30 days for the first 30 days (PDF)

AUTHOR INFORMATION

Corresponding Author

Qiuming Yu — Department of Chemical Engineering, University of Washington, Seattle, Washington 98195, United States; orcid.org/0000-0002-2401-4664; Phone: 206-543-4807; Email: qyu@uw.edu; Fax: 206-685-3451

Authors

Erjin Zheng — Department of Chemical Engineering, University of Washington, Seattle, Washington 98195, United States;
orcid.org/0000-0002-0576-5614

Zhiyin Niu – Department of Chemical Engineering, University of Washington, Seattle, Washington 98195, United States

Gabriella A. Tosado — Department of Chemical Engineering, University of Washington, Seattle, Washington 98195, United States

Hao Dong — Department of Chemical Engineering, University of Washington, Seattle, Washington 98195, United States;

orcid.org/0000-0002-7383-9523

Yaqoub Albrikan — Department of Chemical Engineering, University of Washington, Seattle, Washington 98195, United States Complete contact information is available at: https://pubs.acs.org/10.1021/acs.jpcc.0c05357

Notes

The authors declare no competing financial interest.

ACKNOWLEDGMENTS

This work was partially supported by the National Science Foundation (CBET-1748101 and CMMI-1661660) and the Defense Threat Reduction Agency (HDTRA 1-15-1-0021). E.Z. acknowledges the support from the State of Washington through the University of Washington Clean Energy Institute and via funding from the Washington Research Foundation. Part of this work was conducted at the Molecular Analysis Facility, a National Nanotechnology Coordinated Infrastructure (NNCI) site at the University of Washington, which is supported in part by funds from the NSF (EECS-1542101). UV—vis absorption measurements were carried out in the UW Department of Chemistry's Spectroscopic and Analytical Instrumentation facility. EQE measurements were performed in Prof. Alex Jen group in the Department of Material Science Engineering at the University of Washington.

REFERENCES

- (1) Liu, M. Z.; Johnston, M. B.; Snaith, H. J. Efficient Planar Heterojunction Perovskite Solar Cells by Vapour Deposition. *Nature* **2013**, *501*, 395–398.
- (2) Chen, J. H.; Zuo, L. J.; Zhang, Y. Z.; Lian, X. M.; Fu, W. F.; Yan, J. L.; Li, J.; Wu, G.; Li, C. Z.; Chen, H. Z. High-Performance Thickness Insensitive Perovskite Solar Cells with Enhanced Moisture Stability. *Adv. Energy Mater.* **2018**, *8*, 1800438.
- (3) Zhao, J. J.; Zheng, X. P.; Deng, Y. H.; Li, T.; Shao, Y. C.; Gruverman, A.; Shield, J.; Huang, J. S. Is Cu a Stable Electrode Material in Hybrid Perovskite Solar Cells for a 30-Year Lifetime? *Energy Environ. Sci.* **2016**, *9*, 3650–3656.
- (4) Christians, J. A.; Miranda Herrera, P. A.; Kamat, P. V. Transformation of the Excited State and Photovoltaic Efficiency of CH₃NH₃PbI₃ Perovskite upon Controlled Exposure to Humidified Air. *J. Am. Chem. Soc.* **2015**, *137*, 1530–1538.
- (5) Song, Z. N.; Abate, A.; Watthage, S. C.; Liyanage, G. K.; Phillips, A. B.; Steiner, U.; Graetzel, M.; Heben, M. J. Perovskite Solar Cell Stability in Humid Air: Partially Reversible Phase Transitions in the PbI₂-CH₃NH₃I-H₂O System. *Adv. Energy Mater.* **2016**, *6*, 1600846.
- (6) Conings, B.; Drijkoningen, J.; Gauquelin, N.; Babayigit, A.; D'Haen, J.; D'Olieslaeger, L.; Ethirajan, A.; Verbeeck, J.; Manca, J.; Mosconi, E.; et al. Intrinsic Thermal Instability of Methylammonium Lead Trihalide Perovskite. *Adv. Energy Mater.* **2015**, *5*, 1500477.
- (7) Stoumpos, C. C.; Malliakas, C. D.; Kanatzidis, M. G. Semiconducting Tin and Lead Iodide Perovskites with Organic Cations: Phase Transitions, High Mobilities, and Near-Infrared Photoluminescent Properties. *Inorg. Chem.* **2013**, *52*, 9019–9038.
- (8) Juarez-Perez, E. J.; Hawash, Z.; Raga, S. R.; Ono, L. K.; Qi, Y. B. Thermal degradation of CH₃NH₃PbI₃ perovskite into NH₃ and CH₃I gases observed by coupled thermogravimetry-mass spectrometry analysis. *Energy Environ. Sci.* **2016**, *9*, 3406–3410.
- (9) Weller, M. T.; Weber, O. J.; Frost, J. M.; Walsh, A. Cubic Perovskite Structure of Black Formamidinium Lead Iodide, alpha-HC(NH₂)₂PbI₃, at 298 K. *J. Phys. J. Phys. Chem. Lett.* **2015**, *6*, 3209–3212
- (10) Jeon, N. J.; Noh, J. H.; Yang, W. S.; Kim, Y. C.; Ryu, S.; Seo, J.; Seok, S. I. Compositional Engineering of Perovskite Materials for High-Performance Solar Cells. *Nature* **2015**, *517* (7535), 476.
- (11) Li, Z.; Yang, M. J.; Park, J. S.; Wei, S. H.; Berry, J. J.; Zhu, K. Stabilizing Perovskite Structures by Tuning Tolerance Factor: Formation of Formamidinium and Cesium Lead Iodide Solid-State Alloys. *Chem. Mater.* **2016**, *28*, 284–292.

- (12) Yu, Y.; Wang, C. L.; Grice, C. R.; Shrestha, N.; Chen, J.; Zhao, D. W.; Liao, W. Q.; Cimaroli, A. J.; Roland, P. J.; Ellingson, R. J.; et al. Improving the Performance of Formamidinium and Cesium Lead Triiodide Perovskite Solar Cells using Lead Thiocyanate Additives. *ChemSusChem* **2016**, *9*, 3288–3297.
- (13) Yi, C. Y.; Luo, J. S.; Meloni, S.; Boziki, A.; Ashari-Astani, N.; Gratzel, C.; Zakeeruddin, S. M.; Rothlisberger, U.; Gratzel, M. Entropic Stabilization of Mixed A-Cation ABX₃ Metal Halide Perovskites for High Performance Perovskite Solar Cells. *Energy Environ. Sci.* **2016**, *9*, 656–662.
- (14) Huang, J. H.; Xu, P.; Liu, J.; You, X. Z. Sequential Introduction of Cations Deriving Large-Grain $Cs_xFA_{1-x}PbI_3$ Thin Film for Planar Hybrid Solar Cells: Insight into Phase-Segregation and Thermal-Healing Behavior. *Small* **2017**, *13*, 1603225.
- (15) Liu, T. H.; Zong, Y. X.; Zhou, Y. Y.; Yang, M. J.; Li, Z.; Game, O. S.; Zhu, K.; Zhu, R.; Gong, Q. H.; Padture, N. P. High-Performance Formamidinium-Based Perovskite Solar Cells via Microstructure-Mediated delta-to-alpha Phase Transformation. *Chem. Mater.* 2017, 29, 3246–3250.
- (16) Troughton, J.; Gasparini, N.; Baran, D. Cs_{0.15}FA_{0.85}PbI₃ Perovskite Solar Cells for Concentrator Photovoltaic Applications. *J. Mater. Chem. A* **2018**, *6*, 21913–21917.
- (17) Lee, J. W.; Kim, D. H.; Kim, H. S.; Seo, S. W.; Cho, S. M.; Park, N. G. Formamidinium and Cesium Hybridization for Photo- and Moisture-Stable Perovskite Solar Cell. *Adv. Energy Mater.* **2015**, *5*, 1501310.
- (18) Park, Y. H.; Jeong, I.; Bae, S.; Son, H. J.; Lee, P.; Lee, J.; Lee, C. H.; Ko, M. J. Inorganic Rubidium Cation as an Enhancer for Photovoltaic Performance and Moisture Stability of HC(NH₂)₂PbI₃ Perovskite Solar Cells. *Adv. Funct. Mater.* **2017**, 27, 1605988.
- (19) Zhang, M.; Yun, J. S.; Ma, Q. S.; Zheng, J. H.; Lau, C. F. J.; Deng, X. F.; Kim, J.; Kim, D.; Seidel, J.; Green, M. A.; et al. High-Efficiency Rubidium-Incorporated Perovskite Solar Cells by Gas Quenching. ACS Energy Lett. 2017, 2, 438–444.
- (20) Turren-Cruz, S. H.; Hagfeldt, A.; Saliba, M. Methylammonium-Free, High-Performance, and Stable Perovskite Solar Cells on a Planar Architecture. *Science* **2018**, *362*, 449.
- (21) Knight, A. J.; Wright, A. D.; Patel, J. B.; McMeekin, D. P.; Snaith, H. J.; Johnston, M. B.; Herz, L. M. Electronic Traps and Phase Segregation in Lead Mixed-Halide Perovskite. *ACS Energy Lett.* **2019**, *4*, 75–84.
- (22) Brivio, F.; Caetano, C.; Walsh, A. Thermodynamic Origin of Photoinstability in the $CH_3NH_3Pb(I_{1-x}Br_x)_3$ Hybrid Halide Perovskite Alloy. *J. Phys. Chem. Lett.* **2016**, *7*, 1083–1087.
- (23) Bischak, C. G.; Hetherington, C. L.; Wu, H.; Aloni, S.; Ogletree, D. F.; Limmer, D. T.; Ginsberg, N. S. Origin of Reversible Photoinduced Phase Separation in Hybrid Perovskites. *Nano Lett.* **2017**, *17*, 1028–1033.
- (24) Kubicki, D. J.; Prochowicz, D.; Hofstetter, A.; Zakeeruddin, S. M.; Gratzel, M.; Emsley, L. Phase Segregation in Cs-, Rb- and K-Doped Mixed-Cation (MA)_x(FA)_{1-x}Pbl₃ Hybrid Perovskites from Solid-State NMR. *J. Am. Chem. Soc.* **2017**, *139*, 14173–14180.
- (25) Lin, Y.; Chen, B.; Fang, Y.; Zhao, J.; Bao, C.; Yu, Z.; Deng, Y.; Rudd, P. N.; Yan, Y.; Yuan, Y.; Huang, J.; et al. Excess Charge-Carrier Induced Instability of Hybrid Perovskites. *Nat. Commun.* **2018**, *9*, 1–9
- (26) Ran, C. X.; Xu, J. T.; Gao, W. Y.; Huang, C. M.; Dou, S. X. Defects in Metal Triiodide Perovskite Materials towards High-Performance Solar Cells: Origin, Impact, Characterization, and Engineering. *Chem. Soc. Rev.* **2018**, *47*, 4581–4610.
- (27) Ball, J. M.; Petrozza, A. Defects in Perovskite-Halides and Their Effects in Solar Cells. *Nat. Energy* **2016**, *1*, 1–13.
- (28) Yuan, Y. B.; Huang, J. S. Ion Migration in Organometal Trihalide Perovskite and Its Impact on Photovoltaic Efficiency and Stability. *Acc. Chem. Res.* **2016**, 49, 286–293.
- (29) Khadka, D. B.; Shirai, Y.; Yanagida, M.; Miyano, K. Degradation of Encapsulated Perovskite Solar Cells Driven by Deep Trap States and Interfacial Deterioration. *J. Mater. Chem. C* **2018**, *6*, 162–170.

- (30) Wei, D.; Wang, T. Y.; Ji, J.; Li, M. C.; Cui, P.; Li, Y. Y.; Li, G. Y.; Mbengue, J. M.; Song, D. D. Photo-Induced Degradation of Lead Halide Perovskite Solar Cells Caused by the Hole Transport Layer/Metal Electrode Interface. *J. Mater. Chem. A* **2016**, *4*, 1991–1998.
- (31) Guerrero, A.; You, J.; Aranda, C.; Kang, Y. S.; Garcia-Belmonte, G.; Zhou, H.; Bisquert, J.; Yang, Y. Interfacial Degradation of Planar Lead Halide Perovskite Solar Cells. *ACS Nano* **2016**, *10*, 218–224.
- (32) Wang, R.; Mujahid, M.; Duan, Y.; Wang, Z. K.; Xue, J. J.; Yang, Y. A Review of Perovskites Solar Cell Stability. *Adv. Funct. Mater.* **2019**, 29 (25), 1808843.
- (33) Li, Z.; Lin, J. D. A.; Phan, H.; Sharenko, A.; Proctor, C. M.; Zalar, P.; Chen, Z. H.; Facchetti, A.; Nguyen, T. Q. Competitive Absorption and Inefficient Exciton Harvesting: Lessons Learned from Bulk Heterojunction Organic Photovoltaics Utilizing the Polymer Acceptor P(NDI2OD-T2). Adv. Funct. Mater. 2014, 24, 6989–6998.
- (34) Hu, Y. H.; Ayguler, M. F.; Petrus, M. L.; Bein, T.; Docampo, P. Impact of Rubidium and Cesium Cations on the Moisture Stability of Multiple-Cation Mixed-Halide Perovskites. *ACS Energy Lett.* **2017**, *2*, 2212–2218
- (35) Turren-Cruz, S. H.; Saliba, M.; Mayer, M. T.; Juarez-Santiesteban, H.; Mathew, X.; Nienhaus, L.; Tress, W.; Erodici, M. P.; Sher, M. J.; Bawendi, M. G.; et al. Enhanced Charge Carrier Mobility and Lifetime Suppress Hysteresis and Improve Efficiency in Planar Perovskite Solar Cells. *Energy Environ. Sci.* 2018, 11, 78–86.
- (36) Prasanna, R.; Gold-Parker, A.; Leijtens, T.; Conings, B.; Babayigit, A.; Boyen, H. G.; Toney, M. F.; McGehee, M. D. Band Gap Tuning via Lattice Contraction and Octahedral Tilting in Perovskite Materials for Photovoltaics. *J. Am. Chem. Soc.* **2017**, *139*, 11117–11124.
- (37) Yin, W. J.; Shi, T. T.; Yan, Y. F. Unusual Defect Physics in CH₃NH₃PbI₃ Perovskite Solar Cell Absorber. *Appl. Phys. Lett.* **2014**, *104*, 4.
- (38) Wang, Q.; Shao, Y. C.; Xie, H. P.; Lyu, L.; Liu, X. L.; Gao, Y. L.; Huang, J. S. Qualifying Composition Dependent p and n Self-Doping in CH₃NH₃PbI₃. *Appl. Phys. Lett.* **2014**, *105*, 5.
- (39) Meggiolaro, D.; Motti, S. G.; Mosconi, E.; Barker, A. J.; Ball, J.; Perini, C. A. R.; Deschler, F.; Petrozza, A.; De Angelis, F. Iodine Chemistry Determines the Defect Tolerance of Lead-Halide Perovskites. *Energy Environ. Sci.* **2018**, *11*, 702–713.
- (40) Yang, W. S.; Noh, J. H.; Jeon, N. J.; Kim, Y. C.; Ryu, S.; Seo, J.; Seok, S. I. High-Performance Photovoltaic Perovskite Layers Fabricated through Intramolecular Exchange. *Science* **2015**, 348, 1234–1237.
- (41) Jeon, N. J.; Noh, J. H.; Kim, Y. C.; Yang, W. S.; Ryu, S.; Seok, S. I. Solvent Engineering for High-Performance Inorganic-Organic Hybrid Perovskite Solar Cells. *Nat. Mater.* **2014**, *13*, 897–903.
- (42) Yang, S. D.; Liu, W. Q.; Zuo, L. J.; Zhang, X. Q.; Ye, T.; Chen, J. H.; Li, C. Z.; Wu, G.; Chen, H. Z. Thiocyanate Assisted Performance Enhancement of Formamidinium based Planar Perovskite Solar Cells through a Single One-Step Solution Process. *J. Mater. Chem. A* 2016, 4, 9430–9436.
- (43) Kato, Y.; Ono, L. K.; Lee, M. V.; Wang, S. H.; Raga, S. R.; Qi, Y. B. Silver Iodide Formation in Methyl Ammonium Lead Iodide Perovskite Solar Cells with Silver Top Electrodes. *Adv. Mater. Interfaces* **2015**, 2 (6), 1500195.
- (44) Lee, H.; Lee, C. Analysis of Ion-Diffusion-Induced Interface Degradation in Inverted Perovskite Solar Cells via Restoration of the Ag Electrode. *Adv. Energy Mater.* **2018**, *8*, 1702197.
- (45) Li, J. W.; Dong, Q. S.; Li, N.; Wang, L. D. Direct Evidence of Ion Diffusion for the Silver-Electrode-Induced Thermal Degradation of Inverted Perovskite Solar Cells. *Adv. Energy Mater.* **2017**, *7* (8), 1602922.
- (46) Albadri, A.; Yadav, P.; Alotaibi, M.; Arora, N.; Alyamani, A.; Albrithen, H.; Dar, M. I.; Zakeeruddin, S. M.; Gratzel, M. Unraveling the Impact of Rubidium Incorporation on the Transport-Recombination Mechanisms in Highly Efficient Perovskite Solar Cells by Small-Perturbation Techniques. *J. Phys. Chem. C* **2017**, *121*, 24903—24908.

- (47) Hu, Y. H.; Hutter, E. M.; Rieder, P.; Grill, I.; Hanisch, J.; Ayguler, M. F.; Hufnagel, A. G.; Handloser, M.; Bein, T.; Hartschuh, A.; et al. Understanding the Role of Cesium and Rubidium Additives in Perovskite Solar Cells: Trap States, Charge Transport, and Recombination. *Adv. Energy Mater.* **2018**, 8 (11), 1703057.
- (48) Correa-Baena, J. P.; Luo, Y. Q.; Brenner, T. M.; Snaider, J.; Sun, S. J.; Li, X. Y.; Jensen, M. A.; Hartono, N. T. P.; Nienhaus, L.; Wieghold, S.; et al. Homogenized Halides and Alkali Cation Segregation in Alloyed Organic-Inorganic Perovskites. *Science* **2019**, 363, 627.
- (49) Zhao, C.; Chen, B. B.; Qiao, X. F.; Luan, L.; Lu, K.; Hu, B. Revealing Underlying Processes Involved in Light Soaking Effects and Hysteresis Phenomena in Perovskite Solar Cells. *Adv. Energy Mater.* **2015**, *5*, 1500279.
- (50) Chen, B.; Rudd, P. N.; Yang, S.; Yuan, Y. B.; Huang, J. S. Imperfections and their passivation in halide perovskite solar cells. *Chem. Soc. Rev.* **2019**, *48*, 3842–3867.